

See discussions, stats, and author profiles for this publication at: <https://www.researchgate.net/publication/51859447>

Dynamical Arrest, Percolation, Gelation, and Glass Formation in Model Nanoparticle Dispersions with Thermoreversible Adhesive Interactions

ARTICLE *in* LANGMUIR · DECEMBER 2011

Impact Factor: 4.46 · DOI: 10.1021/la2035054 · Source: PubMed

CITATIONS

32

READS

79

4 AUTHORS, INCLUDING:



[Ramon Castaneda-Priego](#)

Universidad de Guanajuato

61 PUBLICATIONS 639 CITATIONS

SEE PROFILE



[Jung Min Kim](#)

PepsiCo Inc.

7 PUBLICATIONS 67 CITATIONS

SEE PROFILE



[Norman Joseph Wagner](#)

University of Delaware

313 PUBLICATIONS 7,135 CITATIONS

SEE PROFILE

Dynamical Arrest, Percolation, Gelation, and Glass Formation in Model Nanoparticle Dispersions with Thermoreversible Adhesive Interactions

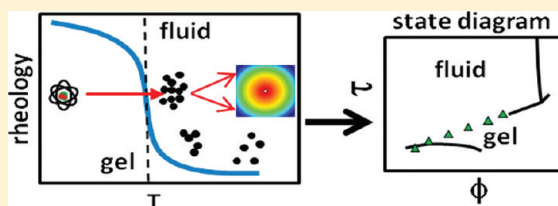
Aaron P. R. Eberle,^{‡,†} Ramón Castañeda-Priego,^{‡,§} Jung M. Kim,[‡] and Norman J. Wagner^{*,‡}

[‡]Center for Neutron Science, Department of Chemical Engineering, University of Delaware, Newark, Delaware 19716, United States

[†]NIST Center for Neutron Research, National Institute of Standards and Technology, Gaithersburg, Maryland 20899, United States

[§]División de Ciencias e Ingenierías, Universidad de Guanajuato, Loma del Bosque 103 37150 León, Mexico

ABSTRACT: We report an experimental study of the dynamical arrest transition for a model system consisting of octadecyl coated silica suspended in *n*-tetradecane from dilute to concentrated conditions spanning the state diagram. The dispersion's interparticle potential is tuned by temperature affecting the brush conformation leading to a thermoreversible model system. The critical temperature for dynamical arrest, T^* , is determined as a function of dispersion volume fraction by small-amplitude dynamic oscillatory shear rheology. We corroborate this transition temperature by measuring a power-law decay of the autocorrelation function and a loss of ergodicity via fiber-optic quasi-elastic light scattering. The structure at T^* is measured using small-angle neutron scattering. The scattering intensity is fit to extract the interparticle pair-potential using the Ornstein–Zernike equation with the Percus–Yevick closure approximation, assuming a square-well interaction potential with a short-range interaction (1% of particle diameter).¹ The strength of attraction is characterized using the Baxter temperature² and mapped onto the adhesive hard sphere state diagram. The experiments show a continuous dynamical arrest transition line that follows the predicted dynamical percolation line until $\phi \approx 0.41$ where it subtends the predictions toward the mode coupling theory attractive-driven glass line. An alternative analysis of the phase transition through the reduced second virial coefficient B_2^* shows a change in the functional dependence of B_2^* on particle concentration around $\phi \approx 0.36$. We propose this signifies the location of a gel-to-glass transition. The results presented herein differ from those observed for depletion flocculated dispersion of micrometer-sized particles in polymer solutions, where dynamical arrest is a consequence of multicomponent phase separation, suggesting dynamical arrest is sensitive to the physical mechanism of attraction.



1. INTRODUCTION

The macroscopic behavior of colloidal dispersions can change from a fluid to solid-like state as a result of a nonequilibrium dynamical arrest transition of the disperse phase when either the volume fraction, ϕ , or the interparticle potential, $\Phi(r)$, is varied.^{3,4} For hard spheres (HS), at $\phi \approx 0.58$ dynamical arrest occurs through the “caging” of particles by their nearest neighbors forming a repulsive driven glass (RDG).³ The addition of a short-ranged attraction can relax this constraint and fluidize the dispersion at constant ϕ , while attractions will ultimately lead to a glass and possible multiple glassy states for one dispersion.⁵ In addition, dynamical arrest driven by attraction can occur at much lower ϕ ,^{6–12} although the particle density defining the transition between glass and a gel is ill defined.¹³ Generally speaking, dynamical arrest leading to a macroscopically homogeneous sample in moderately high to low concentrated dispersions $\phi < \sim 0.40$ is often termed “gelation” and is characterized by a network of particles that displays large scale fractal properties without any significant order. Similarly, colloidal glasses are disordered solids.

A short-ranged attraction in a colloidal system will cause structural reordering of the disperse phase. For strengths of

attraction larger than the thermal energy ($k_B T$) larger bodies composed of individual particles form, such as fractal aggregates or cluster.^{14–16} Above a threshold ϕ , these structures will percolate through the system resulting in an infinitely large cluster leading to bulk dynamical arrest.^{6,17,18} It is well established that dynamical arrest can occur in very dilute colloidal systems ($\phi \approx 10^{-4}$) that interact with a relatively large attractive strength and form irreversible bonds.⁶

Three general classes of model systems have been used to study fractal aggregation, flocculation, gelation, and glass formation. One example is charge stabilized colloidal latex with added electrolyte,¹⁹ but other examples exist such as colloidal gold and silica, as well as carbon black.⁷ Typically, the attraction is due to London-van der Waals dispersion forces and flocculation is induced by screening the stabilizing electrostatic repulsive forces from surface charges by the addition of an electrolyte.²⁰ For sufficient electrolyte addition such that repulsive interactions are negligible and in the absence of

Received: September 6, 2011

Revised: December 5, 2011

Published: December 9, 2011



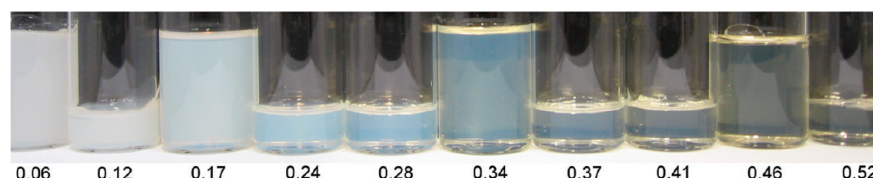


Figure 1. Octadecyl silica dispersion samples of increasing particle concentration from $\phi = 0.06$ to 0.52 at room temperature, $\sim 25^\circ\text{C}$.

significant sedimentation, Brownian motion leads to diffusion limited cluster aggregation (DLCA) with a characteristic fractal dimension $d_f \approx 1.76$.^{14,21,22} However, flocculation due to electrolyte addition is often irreversible and the method does not lend itself to studying the effect of the strength of attraction on dynamical arrest as electrolyte addition changes the rate of aggregation and not the strength of the attractive potential, at least for primary minimum flocculation. Control of the strength of attraction is afforded by depletion flocculation in systems consisting of polymer–colloid mixtures (commonly, polymethylmethacrylate PMMA particles, and linear polystyrene polymer) where the exclusion of the polymer between particles is entropically favorable leading to an effective short-range attraction.²³ The polymer and particles are often treated as a 1-component system where the range Δ and strength U of attraction are related to the polymer radius of gyration, r_g , and concentration, c_p , respectively. However, it is difficult to directly quantify the strength of the potential.²⁴ In addition, phase separation involves significant partitioning of both components and this must be accounted for to quantitatively model the system.^{4,24} Consequently, the state diagram has been shown to depend on the polymer solvent quality,²⁵ and only recently has it been realized that PMMA retains a residual surface charge that can lead to additional structuring in the dispersion.^{26–28} Nonetheless, phase separation and dynamical arrest have been extensively studied in this system, often using confocal microscopy to directly visualize micrometer-sized particles.^{13,29,30} The third type of model system consists of silica dioxide particles with a grafted surface layer of end-tethered octadecane, which has been used for decades as a model system.^{31–34} The interactions between particles are linked to the thermodynamic stability and fluid–solid phase behavior of the thin surface brush layer. The dispersion is sterically stabilized when suspended in good solvents, and will flocculate in poor solvents. In the appropriate solvents where the solvent quality relative to the surface brush changes with temperature, particles will thermoreversibly aggregate.³⁵ Depending on the solvent molecular structure there are two mechanisms for particle aggregation: (1) as solvent quality change leading to a collapse of the stabilizing brush and (2) a liquid-to-solid phase transition of the brush.^{36,37} The first occurs in solvents such as benzene and toluene, where the second occurs in solvent of similar molecular architecture to octadecane such as tetradecane.³⁶ In both cases the collapse of the brush or the brush solidification transition leads to a controllable short-ranged attraction between particles.

Various authors have studied the phase behavior and dynamical arrest transition of octadecyl silica.^{8,10–12,38–41} The results in literature show discrepancies for the strength of attraction necessary for dynamical arrest at low to intermediate volume fractions.^{1,11,12} Grant and Russel¹² measured and fit the structure factor $S(Q)$ from small-angle light scattering in the fluid regime for $\phi < 0.12$ and then extrapolated to the gel-temperature as determined by rheology. Their approach

assumed a linear dependence of the potential on temperature. Verduin and Dhont¹¹ studied the phase transition using various scattering techniques, and defined the dynamical arrest using the point where the light scattering speckle pattern becomes static. This is characteristic of static percolation. Although there is significant disagreement in the strength of the potential necessary for dynamical arrest (gelation) at intermediate volume fractions there is common agreement that below the critical volume fraction ($\phi = 0.266$ for adhesive hard spheres) dynamical arrest occurs for strengths of attraction stronger than required for gas–liquid phase separation.⁴²

Numerous models have been used to explain nonequilibrium dynamical arrest and include but are not limited to percolation,¹⁷ DLCA,⁴³ dynamical arrest,^{44,45} and phase separation;²⁹ for a review see Zaccarelli.¹³ Mode coupling theory (MCT) predicts the dynamical arrest of individual particles⁴⁴ and clusters⁴⁶ to extend from the attractive driven glass (ADG) line to low concentrations. Numerical simulations point toward gelation as a result of an arrested fluid–fluid phase separation which would locate the gel-line within the spinodal region of the state diagram for concentrations below critical.^{13,29} Although our understanding of nonequilibrium arrested phases is growing, clearly there is no consensus concerning dynamical arrest in these model systems.

In this work we experimentally study the dynamical arrest transition from $\phi = 0.06$ to 0.52 using a very well characterized octadecyl silica nanoparticle system. First, we discuss our approach for determining the gel transition using the classic Winter and Chambon⁴⁷ criteria extended to colloidal systems. We confirm the rheological gel-transition as determined from the rheology by fiber-optic quasi-elastic light scattering (FOQELS) and explore the particle dynamics through the transition. The colloidal microstructure is determined by small-angle neutron scattering (SANS). The SANS measurements are fit to extract the interparticle potential at the gel-temperature using the Ornstein–Zernike (OZ) equation with the Percus–Yevick (PY) closure relation assuming a square-well potential with small but finite well width. The potential is mapped on a single interaction parameter, the Baxter temperature, τ , and presented in a state diagram extracted from literature. Finally, we discuss an alternative quantification of the potential at the dynamical arrest transition via the reduced second virial coefficient B_2^* .

2. MATERIALS AND METHODS

2.1. Particle Synthesis and Sample Preparation.

Colloidal silica dioxide nanoparticles were purchased commercially under the trade name Ludox TM-50 (50% mass fraction in H_2O with sodium stabilizing counterion as supplied) from Sigma-Aldrich. Octadecane was covalently grafted to the particle surface via an esterification reaction between the alcohol moieties in 1-octadecanol (97%, Alfa Aesar) and the surface silanol groups following the method of van Helden et al.³² After the reaction, the particles were thoroughly washed

with a 60/40 mixture of chloroform/cyclohexane (chloroform and cyclohexane 99.9%, Fisher Scientific) using a Beckman and Coulter Optima L-100 XP ultracentrifuge. Finally, the particles were stored in cyclohexane; no visual sedimentation was seen after 2 months. Samples were prepared by first drying the octadecyl coated silica under a nitrogen stream and then under vacuum for 24 h. The particles were dispersed in *n*-tetradecane at varying concentrations from dilute through concentrated. The ten concentrations ranging from $0.06 \leq \phi \leq 0.52$ that are the focus of this work are shown in Figure 1 at room temperature (gel state).

2.2. Transmission Electron Microscopy. Images of the coated and uncoated nanoparticles were taken using a JEM-2000FX (LaB6) transmission electron microscope (TEM). The coated particles were imaged prior to cyclohexane/tetradecane solvent transfer. The images were then analyzed using Image J to estimate the mean particle diameter, $\sigma \equiv \sum n_i \sigma_i / n_i$, and polydispersity $PD = s/\sigma$ where s is the standard deviation. For each sample 50 particles were measured.

2.3. Densitometry. The solvent and dispersion density was measured using an Anton Paar DMA-48 densitometer. The solvent density was measured as a function of temperature to ensure an accurate calculation of the scattering length density (SLD) for SANS data analysis. Densitometry on the dispersion was analyzed to determine the particle density in solution. A dilution series was made for each of the silica dioxide particles as received and octadecyl coated particles consisting of 10 dispersions with particle mass fraction $0 \leq X < 0.025$. For the uncoated silica, the stock Ludox ($X = 0.513 \pm 0.006$) was diluted with a 0.1 mM (pH = 9.1 ± 0.1) solution of nanopure H₂O and NaOH to maintain particle stability and match the mother liquor. The octadecyl coated silica was diluted using cyclohexane which is a good solvent for the octadecyl brush. Assuming ideal mixing of the dispersion constituents, the particle density can be extracted using the following equation:

$$\frac{1}{d_{\text{solution}}} = \left(\frac{1}{d_{\text{particles}}} - \frac{1}{d_{\text{solvent}}} \right) X + \left(\frac{1}{d_{\text{solvent}}} \right) \quad (1)$$

where, d_{solution} , $d_{\text{particles}}$, and d_{solvent} is the solution density, particle density, and solvent density, respectively.

2.4. Rheology. Rheological measurements were performed on a TA Instruments AR-G2 stress controlled rheometer with Peltier plate temperature control, and cone-and-plate geometry (40 mm cone diameter, and 2° cone angle) with solvent trap. The temperature of the fluid within the gap was measured and found to be within the instrument accuracy of ± 0.1 °C from the bottom to the top (cone side) of the fluid gap. Conversion between applied and measured parameters (torque M and strain γ) and the rheological material functions were performed using the TA Instruments Rheology Advantage software. For $T > \sim 32$ °C the dispersions fluidize and so thermal annealing can be used to conveniently erase any shear or thermal history. To maintain a consistency between measurements, each sample was subject to the same protocol: The sample was (1) heated to 40 °C and sheared at a shear rate $\dot{\gamma} = 10 \text{ s}^{-1}$ for 2 min, (2) held quiescent at 40 °C for 2 min, and (3) quenched to the measurement temperature for 10 min prior to small-amplitude oscillatory shear (SAOS) measurements. SAOS measurements were performed at a minimum constant stress amplitude $\sigma_0 = 17.68 \text{ mPa}$, in the linear viscoelastic regime to prevent any influence of flow on the development of structure within the system.

2.5. Fiber-Optic Quasi-Elastic Light Scattering. The dynamic motion of the nanoparticles was measured using a Brookhaven Instruments 90Plus fiber-optic quasi-elastic light scattering (FOQELS) with temperature control. The instrument utilizes a 10 mW solid state laser with incident photon wavelength $\lambda = 635 \text{ nm}$ and backscattering correlator positioned at 139°. The temperature was monitored in situ with a calibrated K-type thermocouple (± 0.1 °C). The magnitude of the momentum transfer vector, $Q = |\mathbf{Q}| = 4\pi n_0 / \lambda \sin(\theta/2)$, is fixed, where n_0 is the refractive index of the sample. For this system $Q = 0.025 \text{ nm}^{-1}$, for $n_0 \sim 1.4$ (*n*-tetradecane, $n_0 = 1.429$, and for silica dioxide, $n_0 = 1.456$).⁴⁸ We measured the autocorrelation function (ACF), $g^{(2)}(t) - 1$, between 5 and $10^6 \mu\text{s}$ for dispersion samples up to $\phi = 0.24$. To maintain thermal consistency between rheological and FOQELS measurements the samples were subject to the same thermal protocol discussed above in section 2.4. Measurements were repeated 6 times to ensure reproducibility.

We analyze FOQELS measurements on the dispersions in the neighborhood of the gel transition using a fractal model as follows. For an ergodic system $g^{(2)}(t) - 1$ decays exponentially and can be modeled by $g^{(2)}(t) - 1 = \beta [g^{(1)}(Q, t)]^2$, where $g^{(1)}(Q, t)$ is the dynamic structure factor. For simple diffusion in a monodisperse system, it has the form $g^{(1)}(Q, t) = \exp(-DQ^2t)$.⁴⁹ Here β is a factor related to the instrument and sample geometry. From D the average hydrodynamic diameter can be extracted using the Stokes–Einstein relation $D = k_B T / 6\pi\eta a_h$, where a_h is the hydrodynamic radius. For percolating systems, such as gelling polymer⁵⁰ solutions and colloidal dispersions,^{22,51–53} it has been established both theoretically and experimentally that the autocorrelation function exhibits a transition to a power-law decay near the gel-transition. For such systems, Martin and Wilcox showed^{54,55}

$$g^{(2)}(t) - 1 = \beta^2 \{ A \exp(-DQ^2t) + (1 - A) [1 + (t/t^*)]^{(n-1)/2} \}^2 \quad (2)$$

where A (≤ 1) is a weighting factor, t^* is a time constant, and n is the power-law exponent. The exponential component that is retained in eq 2 accounts for the contribution from the freely diffusing nonaggregated particles. The power-law decay arises from the self-similar structures common to fractal aggregates.⁵⁴

2.6. Small-Angle Neutron Scattering. SANS measurements were performed at the National Institute of Standards and Technology (NIST) Center for Neutron Research (NCNR) in Gaithersburg, MD on both NG3 and NG7 beamlines. Samples were loaded into demountable titanium cells with a 1 mm path length; additional measurements were performed in cells with varying path lengths to explore multiple scattering effects on the scattering profiles. The cell temperatures were maintained to ± 0.1 °C using the 10CB, 10 position sample cell holder with fluid bath. A wide dynamic range in scattering wavevector Q was obtained by combining the sector averaged scattering intensity from three different instrument configurations at detector distances of 1, 4, and 13 m (with focusing lenses at 13 m only). The SANS scattering data was reduced to absolute scale and analyzed with the NIST data reduction and analysis macros in IGOR Pro available from NIST.⁵⁶

The absolute coherent scattering intensity can be modeled as

$$I(Q) = N_p \bar{P}(Q, \rho_i) S(Q) \quad (3)$$

where N_p is the number density of particles, ρ_i is the scattering length density (SLD) of constituent i , and $\bar{P}(Q, \rho_i)$ and $S(Q)$ are the average form factor and structure factor describing the contribution to the scattering intensity from a single particle and the interference from the spatial arrangement of particles, respectively. The particles are modeled using a polydisperse core-shell form factor with a Schultz distribution in particle size.⁵⁶ $S(Q)$ is calculated using the Ornstein-Zernike⁵⁷ (OZ) equation with the Percus-Yevick⁵⁸ (PY) closure approximation scaled by the mean particle diameter.

2.7. Adhesive Hard Sphere Theory. The classic example from statistical mechanics theory of spherical particles interacting via a short-range attraction is that of the AHS fluid first introduced by Baxter.⁵⁹ The Baxter model is an analytical solution to the OZ integral equation with the PY closure approximation for a hard core potential with delta function at the hard core surface. The delta function accounts for an infinitely deep and narrow attraction. Within the framework of this model, the strength of attraction is characterized by a single interaction parameter termed the Baxter temperature, τ , such that as τ decreases the strength of attraction increases. While the Baxter model represents a significant advance there are relatively few real systems for which the potential can be applied. The theory can be extended to a broader number of systems by using an alternate potential with finite width, Δ , and depth, U .² For short-range interactions, $\Delta < 0.1$, the potential can be approximated with the square-well-defined as

$$\Phi(r) = \begin{cases} \infty & r < \sigma \\ -U & \sigma \leq r \leq \sigma + \Delta \\ 0 & r > \sigma + \Delta \end{cases} \quad (4)$$

where $\Phi(r)$ is the pair-potential. The Baxter temperature, τ , can be defined in terms of the square-well parameters and the reduced second virial coefficient, B_2^* , within the framework of integral theory by

$$\tau = \frac{1}{12\varepsilon} \exp\left(\frac{-U}{kT}\right) = \frac{1}{4(1 - B_2^*)} \quad (5)$$

where $\varepsilon = \Delta/(\sigma + \Delta)$.

Cluster formation can be described by specifying the proximity required for particles to be identified as connected. If the center-to-center distance is less than some length (typically $< \sigma + \Delta$) then the two particles are considered "bound". A percolation transition occurs when the cluster size reaches infinity such that there is a continuous network through the system. Using the pair-connectedness function an analytical solution to the dynamic percolation transition has been derived for the Baxter AHS model as¹⁷

$$\tau = \frac{19\phi^2 - 2\phi + 1}{12(1 - \phi)^2} \quad (6)$$

3. RESULTS AND DISCUSSION

3.1. Dispersion Characterization. **3.1.1. Transmission Electron Microscopy.** Transmission electron microscopy images of the uncoated and octadecyl coated silica are shown in Figure 2, panels A and B, respectively. From the images it can be seen that the synthesis procedure for grafting the octadecane to the surface of the silica has no effect on the silica

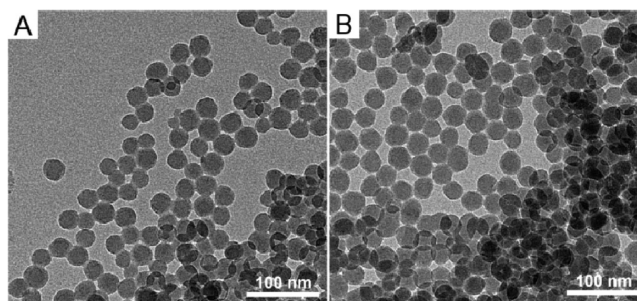


Figure 2. Transmission electron microscopy (TEM) image of (A) the uncoated and (B) octadecyl coated nanoparticles.

core. As a first approximation the particle diameter and variation can be measured from the TEM images. From a population of 50 randomly sampled particles the mean diameter and polydispersity was found to be $\sigma = 27 \pm 7$ nm with PD = 0.1, and $\sigma = 29 \pm 7$ nm with PD = 0.09 for the uncoated and coated particles, respectively.

3.1.2. Densitometry and Estimated Particle Density. Densitometry was performed on both the uncoated particles suspended in 0.1 mM NaOH/H₂O solution, and the coated particles suspended cyclohexane. The experimental results can be seen in Figure 3. The skeletal particle density in solution is

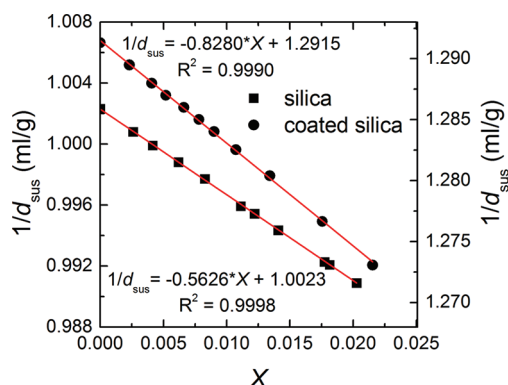


Figure 3. Results of the densitometry experiments for the uncoated (primary y axis, left) and octadecyl coated (secondary y axis, right) nanoparticles. The lines represent a fit of eq 1 to the inverse of the suspension density ($1/\rho_{\text{sus}}$) and the mass fraction (X) of the disperse phase.

extracted from a linear regression of eq 1 to the data and found to be $d = 2.270 \pm 0.001$ and 2.158 ± 0.001 g/cm³ for the uncoated and coated particles, respectively. The reduction in solution density of the coated particles is attributed to the contribution from the surface layer. From neutron contrast variation experiments, published elsewhere,³⁶ we determine the scattering length density (SLD) of the uncoated silica to be 3.553×10^{-6} Å⁻². As the SLD is proportional to the number of atoms per unit volume, it is straightforward to calculate the density from the composition, which gives 2.25 ± 0.01 g/cm³.

The density of the coated silica can be estimated from a mass balance on the silica core and brush layer and the average volume of the particles in solution. The core and shell characteristics have been well characterized by SANS and neutron reflectivity which are reported in detail elsewhere.³⁶ With respect to the core, $\sigma = 28 \pm 0.1$ nm and polydispersity PD = 0.1 ± 0.005 . The particle diameter and polydispersity determined with SANS represents the ensemble average over

the entire scattering volume. This is statistically more accurate than that extracted through the TEM images, and as such these values are used in the successive SANS data analysis discussed later. For the shell, at temperatures above the particle aggregation temperature the brush layer is in a fluid state and has a height $h = 18.5 \pm 0.5$ Å, and solvent concentration $\phi = 0.38$, conversely at low temperatures the brush height and solvent concentration increase to $h = 21 \pm 0.5$ Å and $\phi = 0.46$, respectively. The density of octadecane is $d_{\text{octa}} = 0.7768$ g/cm³ in the fluid state⁴⁸ at 30 °C, and 0.93 g/cm³ as a solid.⁶⁰ The density of the solvent *n*-tetradecane was measured over a temperature range of 25 to 40 °C (data not shown) with linear fit $d_{\text{tetra}}(T) = -7.0 \times 10^{-4}T(^{\circ}\text{C}) + 0.7770$, $R^2 = 0.999$. The total particle density can then be calculated based on a combined fractional density of the core and shell, $d_{\text{coated particle}} = (d^*\phi)_{\text{core}} + (d^*\phi)_{\text{shell}}$. Using this approach, in the fluid state at 30 °C $d_{\text{core-shell}} = 1.79 \pm 0.01$ g/cm³, upon quenching (25 °C) the system, and assuming a maximum brush density of crystalline octadecane, $d_{\text{core-shell}} = 1.80 \pm 0.01$ g/cm³. The lesser of the two was used as an upper bound and the density measured from densitometry was used for the lower bounds for determining the actual particle concentration from fitting SANS measurements, discussed later.

3.2. Rheology. The interparticle potential can be tuned from a HS fluid at high temperatures $T > \sim 32$ °C to an AHS by quenching the system. This, in turn, dramatically changes the nano- and macroscopic structure within the system. We use rheology as a measurement of the bulk mechanical properties which is sensitive to structural changes, and hence, potential.⁶¹ Specifically, we use SAOS rheological measurements to study the temperature dependence on aggregation, thermal and temporal hysteresis, and the dynamical percolation transition of the disperse phase within the system. The interpretation of the rheology is corroborated by scattering techniques in the following section.

3.2.1. Rheological Hysteresis. The temperature dependence of the storage and loss moduli, G' and G'' , respectively, can be seen in Figure 4A for two different temperature ramp rates and direction of ΔT , i.e. heating or quenching the system. At high temperatures, $T > \sim 30$ °C, G' is much smaller than G'' , but at lower temperatures both moduli can rise over 5 orders of magnitude within a narrow temperature window of ~ 2 °C. Inside this window G' becomes greater than G'' indicating the formation of a percolated elastic network that spans the system and is a signature of gelation. The range of absolute temperature over which this occurs depends on the frequency of oscillation, ramp rate, and direction of ΔT . The frequency dependence will be discussed later within this section. As the ramp rate is decreased from 1.0 to 0.1 °C/s both the moduli measured while quenching the system tend toward that measured in the heating cycle. This suggests the system does not reach equilibrium during the ramp rates measured, and clearly indicates a temporal hysteresis of the system. Figure 4B examines this hysteresis further by plotting G' vs time in a constant frequency SAOS measurement where the temperature is either stepped up from 25 °C (gel state) or stepped down from 35 °C (fluid state) to a common temperature. The time required for the moduli to converge increases with increasing final temperature (decreasing potential strength). The storage modulus measured at a common equilibrium temperature merges within a few hundred seconds, but continues to increase even after long times. This rheological aging is thought to be a

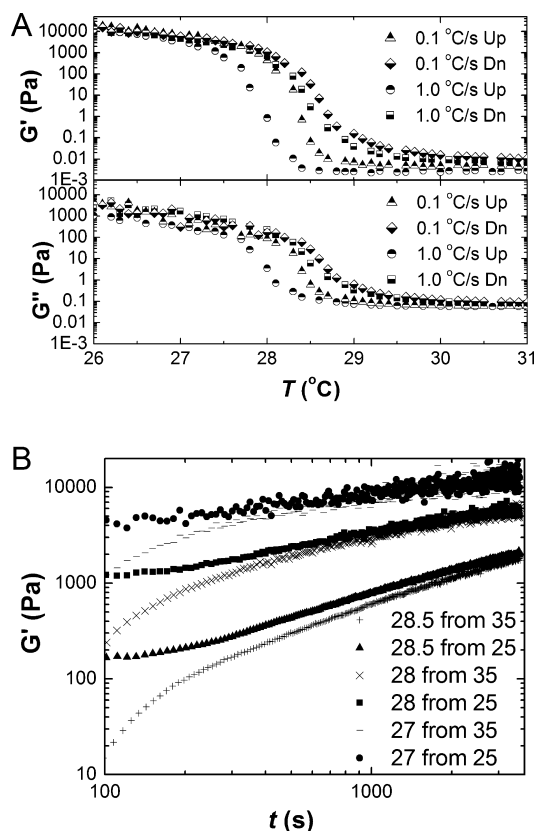


Figure 4. Small-amplitude oscillatory measurements as a function of temperature and time for one dispersion $\phi = 0.28$. (A) Storage G' and loss G'' moduli vs temperature. The ramp rate is given in the figure legend with the direction Up indicating increasing temperature and Dn decreasing. (B) G' vs time in which the temperature has been decreased from 35 °C or increased from 25 °C to the temperature indicated in the legend in units of °C. Data begins at 100s which is the time the temperature reaches equilibrium in the gap. For both figures the measurements were performed at a frequency of $\omega = 2\pi$ rad/s.

result of the slow diffusion of the surface chains interdigitating (see for instance ref 62), but this has yet to be confirmed.

To maintain a consistent structural starting point for experiments a sample conditioning step was performed which included heating the sample above 40 °C (see section 2.4) prior to quenching the system to the desired temperature. Figure 4A suggests that one should start from a temperature below the transition region and heat the system,⁶³ but this approach proved to be inconsistent for more dilute samples $\phi \leq 0.10$ where fragile networks can collapse. Furthermore, it was imperative to quench from the fluid side of the state diagram as this work relies on liquid theory to model the structure.

3.2.2. Gel Transition: SAOS. The purpose of the SAOS rheological analysis is to establish the gel temperature for each sample. Following the work of Winter and Chambon⁴⁷ we define the gel transition as the point where the slopes of G' and G'' become 1/2 and equal. Frequency sweep measurements as a function of temperature in 0.1 °C degree increments can be seen in Figure 5 for one dispersion, $\phi = 0.06$, the lowest concentration reported here that forms a stable gel. For $T \geq 28.1$ °C G' and G'' have a slope of 2 and 1, respectively, on a log–log plot, as expected for a dilute dispersion in this frequency window (i.e., terminal viscoelastic behavior). At lower temperatures G' becomes increasingly dominant, and the slope (defined in the graph as dy/dx) decreases from dy/dx

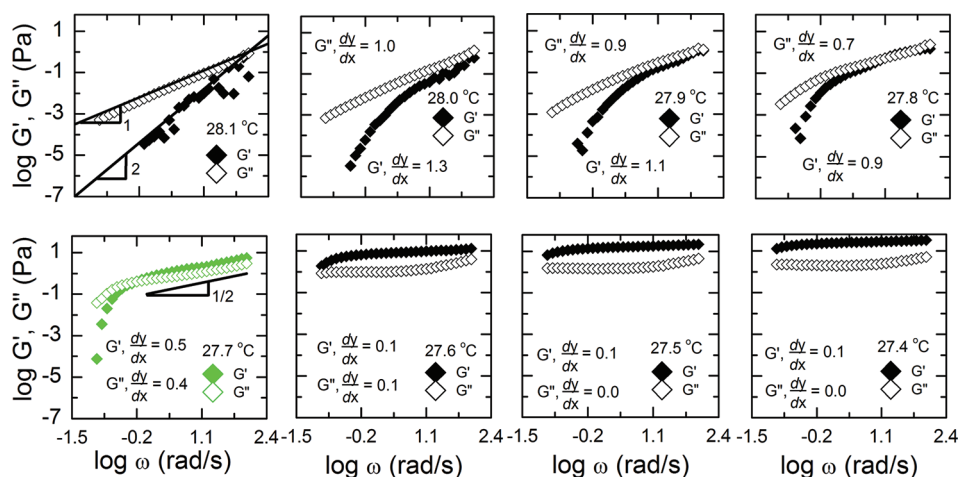


Figure 5. Temperature dependence of the storage (G' , closed symbols) and loss (G'' , open symbols) moduli for one dispersion concentration, $\phi = 0.06$. Within each plot the slopes, dy/dx , of G' and G'' in the range of $\log \omega > -0.2$ are given.

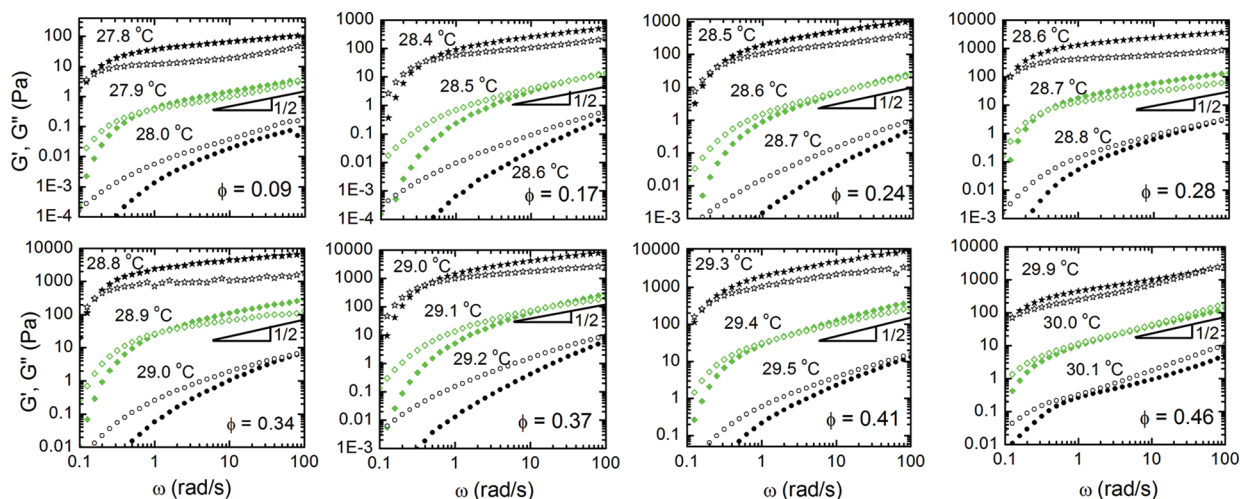


Figure 6. Storage (G' , closed symbols) and loss (G'' , open symbols) moduli from frequency sweep measurements at temperatures around the gel temperature (center, green symbols). Data is offset vertically for clarity by a factor of 0.1 and 10 for the temperatures above the gel and below the gel temperature (green symbols), respectively.

Table 1. Experimental Material Properties for Each Sample, where d_f is the Fractal Dimension

ϕ ($\pm 5\%$)	0.06	0.09	0.12	0.17	0.24	0.28	0.34	0.37	0.41	0.46	0.52
T^* ($^{\circ}\text{C}$) (± 0.1)	27.7	27.9	28.2	28.5	28.6	28.7	28.9	29.1	29.4	30.0	30.8
d_f (FOQELS) (± 0.05)	1.9	2.0	1.8	1.9	1.9						
d_f (SANS) (± 0.05)	2.0	1.9	1.7	1.4	1.0						
H_{shell} (\AA) fluid (± 1)	18.5	18.5	18.5	18.5	18.5	18.5	18.5	18.5	17	17	17
H_{shell} (\AA) gel (± 1)	21	21	21	21	21	21	20	18	17	17	17
τ (fluid) ($\pm 5\%$)	0.130	0.19	0.27	0.4	0.45	0.75	0.76	1.1	1.2	1.6	1.8
τ (gel) ($\pm 7\%$)		0.096	0.102	0.132	0.19	0.28	0.36	0.55	0.75	0.9	1.1

(G') = 2 at 28.1 $^{\circ}\text{C}$ to 0.1 at 27.6 $^{\circ}\text{C}$. At 27.7 $^{\circ}\text{C}$ the slope of G' is equal to 1/2 for $\omega > 0.5$ rad/s and is nearly equal to the slope of dy/dx (G'') = 0.4 at the same temperature. Following the classic analysis of Winter and Chambon,⁴⁷ we define this temperature to be the gel temperature. At the lowest frequencies within the experimental window, $\omega < 0.5$ rad/s, there is terminal viscoelastic behavior in both G' and G'' associated with a relaxation within the system, which is expected for a physical gel and stands in contrast to chemical gels. Note that this well-established rheological definition of the gel temperature is not only precise and reproducible, but also

physically meaningful. The dispersion does not flow at this temperature when a partly filled vial is inverted but will flow when warmed only slightly. However, when left overnight, the dispersion will show evidence of creeping, consistent with physical gelation.

The trend in the temperature dependence of G' and G'' is universal for all the dispersion concentrations discussed here that form a stable gel. This is shown in Figure 6 for eight dispersion concentrations from $\phi = 0.09$ to $\phi = 0.46$. For each case the slopes of both dynamic moduli transition through 1/2

at similar temperatures and marks the point which we define as T^* ; the values are given in Table 1.

3.3. Fiber-Optic Quasi-Elastic Light Scattering. The particle dynamics are measured as a function of temperature using FOQELS to provide a second, independent measurement of T^* for comparison with rheology. It is well established that gelation is a kinetic transition affecting to both self- and collective diffusion.⁶⁴ For small length scales relative to the mean separation distance the scattering probes the self-diffusion, whereas large length scales probe the correlated or collective diffusion. The transition between self- and collective diffusion can be defined through the location of the primary peak in the structure factor that characterizes the mean interparticle spacing. This can be approximated by $Q_p \approx 2\pi/r_{\text{avg}}$, where $r_{\text{avg}} \approx 1/n_p^{1/3}$ is the average particle separation, and $n_p = 3\phi/4\pi a^3$ is the particle number density. In this system $Q_p = 0.10$ and 0.21 \AA^{-1} for $\phi = 0.06$ and 0.24 , respectively. Within the criterion $Q \leq Q_p$ we are probing the collective diffusion of the particles within all the samples. Hence, with this technique we are searching for a thermal transition in the collective diffusion characterized by (i) reduced diffusive motion, (ii) a distribution of relaxation modes, and (iii) a switch in ergodicity.

FOQELS enables measuring the particle dynamics in most of the dispersion concentrations ranging from dilute to concentrated, see Figure 1. This is done by correlating the intensity fluctuations at a backscattering angle of 139° which minimizes multiple scattering effects and beam attenuation from sample turbidity. However, we limit the analysis of the data as there is uncertainty in the contribution of multiple scattering and instead focus on general trends which still persist and provide clear signatures for gelation. The results of the FOQELS measurements presented via the ACF can be seen in Figure 7

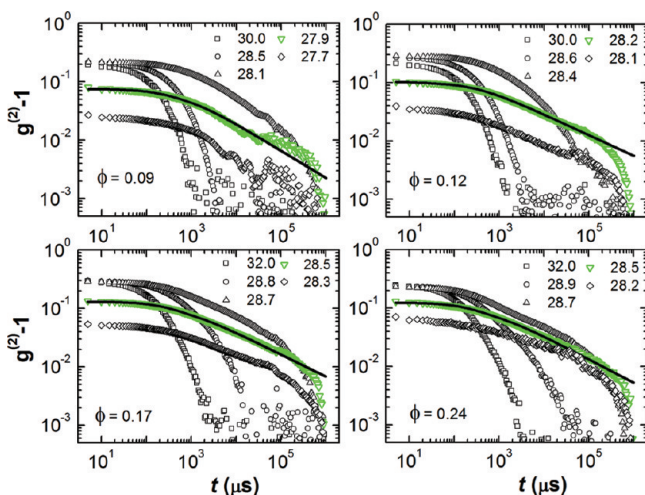


Figure 7. Autocorrelation function vs delay time as a function of temperature near the gel transition. Lines represent a fit of eq 2. The green symbols represent the dynamical transition temperature.

for four dispersion concentrations from $\phi = 0.09$ to 0.24 . For $\phi > 0.24$ the system dynamics show marked changes with temperature but are difficult to interpret within the experimental correlation time window. The general trend of the ACF is similar for all concentrations measured. At high temperatures, $T > \sim 32^\circ \text{C}$ the ACF displays the expected time-decay signifying structural relaxation by particle diffusion. A dilution series was measured at high temperatures and used to extract the hydrodynamic diameter, which agrees well with that

extracted from SANS (data not shown). Upon quenching samples at moderate to high concentrations three distinct changes occur: (i) the exponential decay extends toward longer correlation times, (ii) the ACF develops a power-law decay at long correlation times, and (iii) the magnitude of the plateau at short correlation times decreases. The transition from an exponential decay to a stretched exponential of the form $g^{(1)}(Q, t) = \exp[-DQ^2 t]^\xi$, where ξ is the stretch exponential, is a result of particle clustering broadening the distribution of relaxation modes.⁶⁵ The clusters have a well-defined fractal-like structure that becomes less dense as the aggregate grows in size leading to a power-law spectrum of relaxation times. A power-law decay of the ACF (eq 2) has been shown to be associated with the percolation threshold for polymers,⁵⁰ in irreversible aggregating silica,²² copolymer micelles,⁶⁶ and in thermal silica.⁸ Finally, the decrease in the plateau at $t \rightarrow 0$ is known to be a signature of an ergodic to nonergodic transition, or in this case gelation.^{22,52,53,63} Here we identify the gel transition temperature from FOQELS by evidence of both a power-law decay and the decrease in the plateau intensity. The ACF at the transition temperature is shown in Figure 7 displayed as green triangles. The transition temperature defined by the criteria above agrees within $\pm 0.1^\circ \text{C}$ of the transition temperature measured using rheology, validating the consistency and accuracy of the determination.

The power-law decay of the ACF can be further analyzed with the theory of Martin and Wilcox,^{54,55} (eq 2). Fits of the ACF at the gel transition are shown in Figure 7 (solid line). The fits yield the power-law exponent, n , which is related to the underlying microstructure and can be used to give an estimate of the fractal dimension d_f within the system.²² Models have been proposed for percolating polymers and vary in their assumptions regarding hydrodynamic and excluded volume interactions. One example which relates n and d_f within the assumption of screened excluded volume effects is given by⁶⁷

$$n = \frac{3(5 - 2d_f)}{2(5 - d_f)} \quad (7)$$

Calculation of the fractal dimension based on eq 7 leads to $d_f \approx 2$ for all dispersion concentrations, the values are given in Table 1. This is consistent, within the ability to determine it, with the expected aggregation mechanism of diffusion limited cluster aggregation (DLCA).¹³ In the next section we will compare these results to the d_f extracted from SANS.

3.4. SANS. Small-angle neutron scattering (SANS) is used to characterize both the single particle properties, and the collective structure within the system. The major contribution of this section is to present the method used to extract the interparticle potential through fitting the scattering intensity using liquid theory. In a previous work³⁶ we present a detailed characterization of the silica core, and octadecane shell as the temperature is quenched through the particle aggregation transition, and the results are briefly discussed in section 3.1.2.

The scattering intensity is shown in Figure 8 for two dilute dispersions in the fluid state (40°C) and in the form factor limit, $I(Q) \lim_{\phi \rightarrow 0} \approx N_p \bar{P}(Q, \rho_i)$. The systems have different scattering intensities reflecting different neutron contrast arising from different solvents, one being hydrogenated and the other deuterated. The scattering intensities for $I(Q) > 0.01 \text{ \AA}^{-1}$ are fit by varying ϕ only, bound by limits defined in 3.1.2, with two models using the known material parameters for the core, shell, and solvent: (i) a polydisperse core-shell model that contains

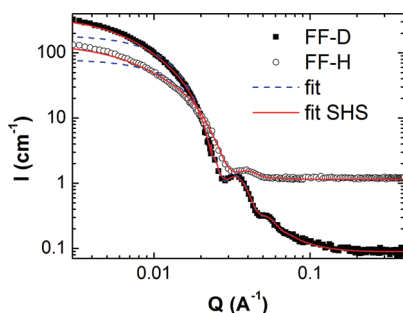


Figure 8. Form factor fits of the scattering intensity in the fluid state (40 °C) for two dilute dispersions, $\phi = 0.006$ and 0.008 , in hydrogenated (FF-H) and deuterated (FF-D) tetradecane, respectively. The blue (broken) line is a fit of the form factor only [i.e., setting $S(Q) = 1$] using a polydisperse core shell model, and the red (solid) line is a fit which includes a finite contribution of structure factor using the adhesive hard sphere model.

only $P(Q)$ with the prefactor (broken line) and (ii) a fit that includes a finite $S(Q)$ contribution using the adhesive hard sphere model (solid line). In the latter, the same material parameters are used for $P(Q)$ only the depth of the potential is varied and not the width (discussed in more detail later). The prediction of the form factor shows excellent agreement for both dispersions up to $Q \approx 0.01 \text{ Å}^{-1}$, after which the predicted intensity plateaus while the measured increases slightly. By including a contribution from $S(Q)$ we are able to fit the intensity over the entire Q range. This shows that even at high temperatures in the fluid state there is a small residual attraction between particles, which is expected as the system is not perfectly refractive index matched.²¹

SANS measurements were performed over a range of temperatures spanning the transition from the fluid state through gelation for all the sample concentrations listed in Table 1. The scattering intensity evolves systematically in the fluid state with decreasing temperature within the same temperature window where marked changes in the rheology and dynamics are evident, until T^* . Near T^* but for $T < T^*$ the scattering intensity no longer evolves but remains constant within experimental uncertainty. This data is presented in Figure 2a of ref 1 and occurs for all samples measured. The constant scattering intensity for $T < T^*$ indicates an arrest of the structure at the length scales accessible by SANS. This is confirmation that the fits of the scattering intensity at T^* are indeed of the structure at the gel transition when quenching from the fluid phase boundary.

We now discuss fitting the SANS scattering intensity for the dispersions in both the fluid state and at the gel transition. In total, the model for predicting the scattering intensity including the prefactor, form factor, and structure factor includes 10 parameters, 6 of which are known from independent experiments and held constant. The perturbation parameter ϵ which defines the square-well width is held fixed for all concentrations at $\epsilon = 0.01$ as it gave the most accurate description of the scattering profiles and is consistent with previous work.^{10,11,34} Furthermore, all fits performed with $\epsilon < 0.1$ gave similar results for the Baxter temperature (which is consistent with the hypothesis of corresponding states for short ranged attractions).⁶⁸ The remaining three parameters include the particle volume fraction ϕ , shell thickness h , and the depth of the potential U . The particle concentration was constrained by the densities discussed in section 3.1.2, and the shell

thickness was constrained by physical considerations to 15–21 Å. Determining a unique set of material parameters by minimizing the sum of the residuals over the entire Q -range is not trivial as each parameter has a convoluted impact on the predicted intensity. However, we employed a rigid protocol utilizing features in the scattering intensity in both the fluid and gel state. In the fluid state the concentration was fit to the primary interaction peak at $Q_p \approx 2\pi/r_{\text{avg}}$. This value was then set fixed for the fit of the intensity at the gel transition. The shell thickness was fit to the trailing edge of the second order peak due to the form factor as it had the greatest effect on the curve in this region. Finally, the potential depth was fit to the low- Q region of the scattering curve. The potential depth was the only unconstrained variable in the fitting.

Multiple scattering can contribute to the intensity for concentrated dispersions and is of concern. The probability of a multiple scattering event depends on various factors which include the neutron contrast, the incoherent cross section of the sample, and the sample path length. For all the samples in which we fit the interparticle potential we used hydrogenated solvent which has a large incoherent scattering cross section ($\sim 80\times$ deuterium). In addition, these samples have a high neutron contrast between the core silica and the solvent ($\Delta\rho \approx 4 \times 10^{-6} \text{ Å}^{-1}$). Both contribute to multiple scattering within the samples and is expected to increase with particle concentration. This can be clearly seen in Figure 9 which shows the scattering

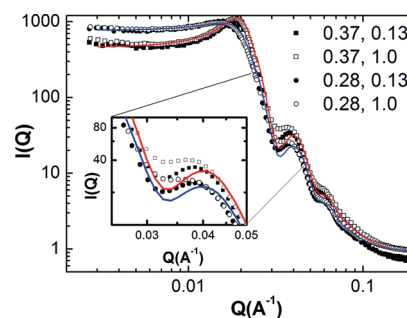


Figure 9. Effect of sample path length on the SANS scattering intensity of two dispersion concentrations $\phi = 0.37$ and 0.28 at 40 °C (fluid state). The scattering curves are shown for two sample path lengths of 0.13 (closed symbols), and 1.0 mm (open symbols). Inset is an expanded view of the primary minimum and secondary peak of the scattering curve showing the effect of multiple scattering.

intensity for two dispersion concentrations of $\phi = 0.37$ and 0.28 in the fluid state (40 °C) measured at two path lengths, 1.0 and 0.13 mm. Assuming there is a linear relationship between the probability of a scattering event and the sample path length, the thickness of the sample is linearly proportional to the amount of the multiple scattering. There are distinct differences between the two curves, but generally, the increase in path length (proportional to the increase in multiple scattering) has a similar effect as an increase in polydispersity in the system. Specifically, features such as the higher order peaks of the form factor are smeared. In addition, there is a clear increase in the incoherent background. Fits of the scattering intensity in the longest path length (open symbols) show good agreement throughout the entire Q -range except for the higher Q peaks of the form factor. The scattering profile at the shorter path length shows even better agreement for the higher Q peaks. Hence, we attribute these specific deviations between the measured and fit intensity values to a small amount of multiple scattering, but we

find multiple scattering has a negligible effect on the fit parameters.

The SANS scattering intensity at the fluid and gel states for all the dispersion concentrations can be seen in Figure 10 (A)

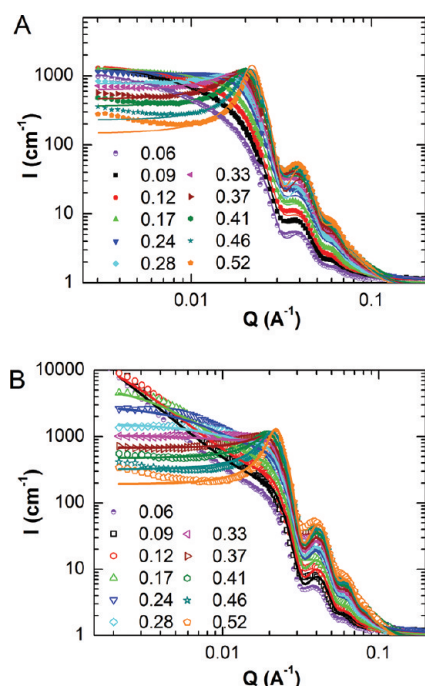


Figure 10. (A and B) Experimental and fit static-SANS scattering intensity, I , vs scattering wavevector, Q , at 40 °C (fluid state) and at the gel point temperature (temperatures not shown), respectively.

and (B). A direct comparison between the scattering intensities in the two states can be seen in Figure 3 of ref.¹ The difference in the scattering intensity between the fluid and gel state systematically decreases with increasing particle density. This is attributed to excluded volume effects, where more dilute dispersion undergo structural reorientation over larger length scales compared to more dense systems. Visually this manifests through sample turbidity which can be seen in Figure 1, an image of the samples in the gel state. The most dilute sample ($\phi = 0.06$) is also the most turbid as the large scale structures have a greater contribution to the scattered light. In a similar manner, for dilute to intermediate concentrations $0.06 \leq \phi \leq \sim 0.24$, the SANS scattering intensity exhibits a significant low- Q rise in intensity, that can be related to a fractal dimension and correlation length of the fractal repeat unit. The fractal dimension can be determined experimentally from the Q dependence of the scattering intensity, $I(Q) \approx Q^{d_f}$ for $QR_g > 1$.⁶⁹ Ideally, the low- Q curve should be fit over a minimum of a decade in Q . For the most dilute we are able to fit an entire decade but for higher concentrations the cut off by the low- Q plateau reduces the fractal regime of scattering intensity. The results of fits to the fractal scattering regime are presented in Table 1. For the most dilute concentration ($\phi = 0.06$) $d_f = 2.0$ which agrees well with the fractal dimension extracted from fitting the FOQELS data. For higher concentrations d_f decreases linearly with concentration, whereas the values extracted from FOQELS maintain $d_f \approx 1.9$. Note that SANS and FOQELS are probing very different ranges of structure and are fundamentally different in what they measure (static structure versus relaxation spectra) so this difference at

moderate concentrations is not unexpected, but has not been explored in the literature.

Fits of the SANS scattering intensity for all the samples in the fluid state (40 °C) and at T^* can be seen in Figure 10, panels A and B. As a note, we were unable to fit the most dilute sample $\phi = 0.06$ as the theory becomes unstable for low- ϕ at low τ values. The values for the fit parameters can be seen in Table 1. In general, the fits show good agreement over the entire Q -range. There are deviations in two regions: (i) at the higher order form factor peaks the deviation increases with particle concentration, which as discussed is attributed to multiple scattering, and (ii) the low- Q region of the two highest concentrations. The highest concentrations are the most difficult for liquid theory to model, but even in this case it should not have a large impact of the fit parameters. It is also possible that this deviation at low- Q represents a contribution from some heterogeneities, which are known to exist in colloidal glasses.⁷⁰

The best fit parameters for the shell thickness h were identical to that found in ref 36 for $\phi \leq 0.28$. For $\phi > 0.28$ the best fit value for the shell height in the gel state decreased to a minimum of 17 Å. In the fluid state the values were consistent for $\phi \leq 0.37$ and for higher concentrations converged on 17 Å. The change in shell thickness with increasing concentration is consistent with expected overlapping of the brush layer as the particles are crowded together at higher concentrations. A similar argument can be made for the fluid state, where now the brush is solvated and acts to stabilize the particles.^{71,72}

3.5. State Diagram. The experimentally determined interparticle potential at the fluid-gel transition is presented in a state diagram in Figure 11 along with literature data for

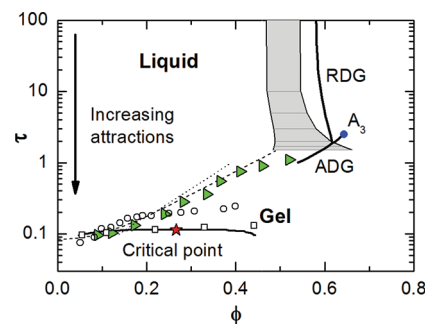


Figure 11. State diagram for the model adhesive hard sphere system (AHS). (—) Is the liquid–vapor coexistence region with critical point (red star, $\tau_c = 0.1133$ and $\phi_c = 0.266$) as determined by Monte Carlo (MC) simulation;⁴² the broken line is the analytical solution to the percolation line using the Percus–Yevick approximation, eq 6, which extends to the liquid–crystal coexistence region;¹⁷ dotted line is the MC simulation of the percolation transition;⁷³ gray shaded region is the liquid–crystal coexistence region from the modified weighted-density approximation (MWDA) theory;⁷⁴ (—) repulsive and attractive driven glass (RDG and ADG) lines from model coupling theory (MCT) with point singularity, A_3 (blue circle), shifted to higher particle densities from experimental data.⁷⁵ (○) and (□) are the experimental percolation points of Verduin and Dhont and gel transition of Grant and Russel,¹² respectively. The green triangles are the experimentally determined dynamical arrest transition from this work.

accepted state and phase transitions for the AHS system, and previous experimental results. At low ϕ and high attractive strength (low τ) there is a liquid–vapor coexistence region with critical point at $\tau_c = 0.1133$ and $\phi_c = 0.266$ (star) predicted by

MC simulations.⁴² Conversely, at high ϕ and weak attractions there is a liquid crystal coexistence region calculated from modified weighted-density approximation theory.⁷⁴ For monodisperse systems the liquid-crystal coexistence line extends to more dilute volume fractions but it is well-known that polydispersity impedes crystallization.⁷⁶ This is in addition to a RDG line which intersects the ADG line with mode-coupling theory singularity A_3 .⁷⁵ As is typically done, the location of the RDG and ADG lines calculated from MCT are shifted to higher particle densities by using known experimental data as the MCT under predicts the RDG line.³ The dynamic percolation line as calculated by the pair-connectedness function within the PY approximation, eq 6, can be seen extending from the liquid–vapor coexistence region at low- ϕ to the liquid-crystal coexistence region at high- ϕ .¹⁷ In addition, the percolation transition as predicted by MC simulations can be seen following a similar ϕ dependence as the theory.⁷³ The experimentally determined points which bound the dynamical arrest transition (triangles) correspond closely to percolation theory up to $\phi = 0.41$. For $\phi > 0.41$ the boundary tends toward the MCT ADG line. This represents a major contribution of this work: namely, that for the AHS nanoparticle system the dynamical arrest (gelation) transition extends from the dilute particle concentration side of the liquid–vapor coexistence and above the critical point following predictions of percolation theory until at sufficiently high concentrations it subtends to the predictions and joins the MCT ADG line.

The results of the dynamical arrest transition differ quantitatively from previous results by Verduin and Dhont¹¹ and Grant and Russel¹² who studied similar octadecyl-coated silica particles (radii of 38 nm for the former, and 47, 56, and 72 nm for the latter) but in different suspending media (benzene and hexadecane) and with different methods to determine the gel point. Indeed, their methods focus on static percolation (nonergodicity of all particles), as opposed to the determination of the dynamical arrest defined herein (existence of a self-spanning cluster), which is more appropriately connected to the dynamic percolation (as validated experimentally). Their data is also plotted in Figure 11 for comparison. In all cases the data agrees at dilute concentrations where the gel line intersects the liquid–vapor coexistence region. For higher concentrations the results by Grant and Russel show little dependence on ϕ , while that of Verduin and Dhont follow the theoretical percolation transition and corresponds to our data up to $\phi \approx 0.3$. For $\phi > 0.3$ our results diverge. It is likely that the differences are due to the definition of the gel transition, the approach to measuring the strength of attraction, and the solvent. The temperature of dynamical arrest corresponding to the gel transition is defined by Verduin and Dhont as the point where the observed speckle pattern of scattered light becomes static in a light scattering experiment. From measurements of the dynamics seen in Figure 7 it is clear that this definition will lead to a lower T^* than the point of dynamic percolation, which we define here as the dynamical arrest transition. In addition, these authors use benzene as the suspending medium, which changes the molecular mechanism responsible for particle attraction (although it is not clear if this should have any effect on the results).³⁷ In the work of Grant and Russel, the strength of attraction was determined by fitting the low- Q static light scattering results in the fluid region to a linear function of temperature and extrapolated to T^* . This approach led to an even lower τ than that found by Verduin and Dhont and the extrapolation approach was found to be least accurate for their

smallest sized particles. Thus, although it remains unclear why these two prior determinations differ from each other,¹¹ it is consistent with expectation that our determination of dynamic percolation should lie above these determinations of static percolation on the AHS state diagram. It is interesting to speculate about how the gel transition defined by static percolation might merge with the ADG transition, as the ADG would have the same signatures used to determine the static percolation transition. Their experimental data do not extend to sufficiently high concentrations to be definitive, but the data do not appear to extrapolate to the MCT predicted ADG line. This is in contrast to our data, which merge smoothly from the predicted percolation transition to the MCT ADG. We note that gravitational settling may play an important role in comparing measurements, such that particle size may be very important in these experiments.¹⁸ This effect is the subject of ongoing research.

The work presented herein focuses on thermal silica which is a 1-component system where the attraction is a manifestation of a surface molecular phase transition of the brush layer. However, there is a significant body of literature pertaining to depletion aggregation.^{13,29,44,77} The most widely used system being colloid–polymer mixtures where sterically stabilized poly methylmethacrylate (PMMA) is the colloid.¹⁸ In this case entropy drives particle aggregation and acts as an effective attraction between particles in which the strength and range of attraction are controlled by the free volume concentration and polymer size. However, it is nontrivial to quantify experiments as the relation between polymer concentration and potential is complicated by the multicomponent fluid and the conformational states of the polymer in solution.⁷⁸ Furthermore complications arise as colloid–polymer mixtures are bicomponent systems where the polymer phase partitions strongly with the colloidal phase upon aggregation.²⁴ Recently, Lu et al.²⁹ reported that phase separation precedes gelation in PMMA–polymer mixtures and suggests that this mechanism should apply to all AHS systems, which would imply that gelation is fundamentally a jamming transition induced by phase separation rather than a homogeneous dynamical arrest within the fluid. Our gelation transition intersects the predicted phase boundary at $\phi \approx 0.15$, which is slightly higher than observed by Verduin and Dhont and about the same as observed by Grant and Russel. However, our transition lies above the critical point such that gelation for more concentrated systems clearly precedes without phase separation. Indeed, our samples for low concentrations within the predicted two phase region gel without evidence of phase separation, which is consistent with previous reports for nanoparticle dispersions where gelation is fast relative to phase separation.¹¹ Here again the large particle size and different molecular mechanism of inducing the attractive interactions probably plays an important role in explaining the differences in observation.

The potential parameters extracted from experiments using a square-well potential are present in terms of τ in Figure 11. It has been argued through the Noro-Frenkel⁶⁸ extended law of corresponding states that for short-range attractive systems $\Delta < 0.1\sigma$ it is not the shape of the potential that defines the phase behavior but the reduced second virial coefficient B_2^* . As there is a one-to-one correspondence between the Baxter temperature and B_2^* (given by eq 5) our data can also be represented in this form. For reference, $B_2^* = 1$ and $B_2^* = 0$ corresponds to a hard sphere fluid and the definition of the Boyle temperature, respectively. In Figure 12 we plot B_2^* as a function of volume

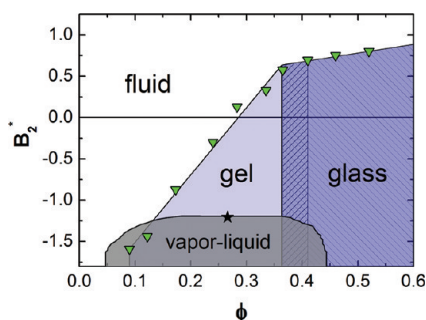


Figure 12. The reduced second virial coefficient B_2^* vs dispersion concentration measured in the fluid state and at the dynamical arrest transition. The vapor–liquid coexistence with critical point is from ref 42.

fraction. In the gel state, B_2^* increases monotonously with concentration for $\phi < \sim 0.4$ and changes in sign from negative at densities below the critical concentration $\phi_c = 0.266$ to positive at higher values (i.e., the Boyle temperature is approximately the critical temperature along the gel line for the critical volume fraction). The significance of sign change of B_2^* in the vicinity of the ϕ_c has yet to be elucidated by theory, but is intriguing as a possible signature of a gel-to-glass transition. For $\phi > \sim 0.4$ the slope of B_2^* changes dramatically and the experimental data subtends the predictions of the percolation prediction. Linear fits of both regions intersect at $\phi \approx 0.36$, and it is in the vicinity of this concentration ($0.36 < \phi < 0.4$) we speculate that there is a change from a gel (as defined by dynamic percolation) to an glass. In the latter case caging by neighboring particles can significantly contribute to dynamical arrest, whereas for more dilute concentrations the formation of fractal-like dynamic aggregates is the known mechanism. The apparently linear dependence of B_2^* on ϕ along the dynamic percolation line has, to our knowledge, not been previously reported. This observation helps to explain the absolute temperature dependence of the gel transition with particle concentration and illustrates the complementary roles played by direct particle energetics (i.e., the AHS attraction and interparticle energy) and particle crowding (excluded volume and entropy); less attraction is required for dynamical arrest as particles are crowded by increasing concentration. Hence, with this work we find that the dynamical arrest transition is dependent on both the strength of attraction and the excluded volume driving forces, and that there is a continuous line from dilute systems, where fractal-like gels form to concentrated glasses.

From Figure 12 it is clear the two most dilute concentrations are buried within the vapor–liquid phase transition, yet experimentally there was no indication of a macroscopic phase separation through visual sedimentation. One explanation is that gel formation resulting in a percolated system is faster than spinodal decomposition.¹¹ It is also possible that the surface molecular brush does interdigitate, which could act as an increase in the surface friction and prevent the formation of dense and large aggregates, which are a characteristic in phase separated systems.²⁹ Particle size effects are thought to be very significant¹⁸ and ongoing studies may shed light on this difference.

4. CONCLUSIONS

In this work we use a model nanoparticle system with thermoreversible interactions to experimentally map out the

dynamical arrest transition of the AHS model for dilute to concentrated conditions. Combining rheology and scattering techniques (FOQELS and SANS) enable establishing the gel temperature with precision and accuracy, and to translate the experimental measurements unambiguously to compare with the model system parameters and existing simulation and theory for the AHS state diagram. Here, T^* is defined using the rheological criterion of Winter and Chambon.⁴⁷ This transition is corroborated quantitatively by independent measurements of the particle dynamics as characterized by an exponential decay of the ACF and an ergodic to nonergodic structural transition. Fits of the SANS scattering intensity at T^* to liquid state theory yields the Baxter temperature corresponding to T^* and enables direct, quantitative comparison to theory for the AHS model system. A continuous dynamical arrest transition extends from the vapor–liquid coexistence region at low- ϕ following the predicted dynamic percolation transition above the critical concentration and occurs without macroscopic phase separation. For $\phi \approx 0.4$ this transition subtends the percolation line and smoothly merges with the predicted attractive driven glass transition. Differences with prior reports for related, but different thermally reversible gelling dispersions can be partly attributed to the difference between dynamic and static percolation. Interestingly, when cast in terms of the second virial coefficient B_2^* our results suggest a change in the contributions to the dynamical arrest transition from that dominated by interparticle interactions to that dominated by excluded volume caging possibly leading to a distinction between a gel and a glass. Based on previous work and our results, it is clear that thermally reversible model AHS systems exhibit a gel transition that falls within the two phase boundary for $\phi < \sim 0.15$. However, we observe gelation without phase separation, which may be a result of using nanoparticles such that gelation is fast relative to phase separation and gravitational forces are not sufficient to enhance phase separation. Future studies will examine the effects of particle size on the gelation and phase separation behavior at low concentrations.

AUTHOR INFORMATION

Corresponding Author

*E-mail: wagnernj@udel.edu. Tel: 302-831-8079. Fax: 302-831-1048.

ACKNOWLEDGMENTS

The authors thank Yun Liu (NIST CNR), Vincent Martinez, and Wilson Poon (University of Edinburg) for discussion. The financial support for this work was partially provided by the National Academy of Science through a National Research Council Postdoctoral Fellowship award (A.P.R.E.), the University of Delaware and NIST Cooperative Agreement #70NANB7H6178, and Conacyt–Mexico (Grants 61418/2007, 102339/2008, and 144518/2010 and NSF–Conacyt Project 147892/2011). We acknowledge support from the NSF for the use of SANS instrumentation, DMR–0944772. The identification of any commercial product or trade name within this paper does not imply recommendation or endorsement by the National Institute of Standards and Technology, nor does it imply that the materials or equipment identified are necessarily the best available for the purpose.

REFERENCES

- (1) Eberle, A; Wagner, N. J.; Castaneda-Priego, R. *Phys. Rev. Lett.* **2011**, *106*, 105704.

- (2) Menon, S. V. G.; Manohar, C.; Rao, K. S. *J. Chem. Phys.* **1991**, *95* (12), 9186–9190.
- (3) Pusey, P. N.; van Megen, W. *Phys. Rev. Lett.* **1987**, *59* (18), 2083–2086.
- (4) Poon, W. C. K.; Selfe, J. S.; Robertson, M. B.; Ilett, S. M.; Pirie, A. D.; Pusey, P. N. *J. Phys. II* **1993**, 1075.
- (5) Pham, K. N.; Puertas, A. M.; Bergenholtz, J.; Egelhaaf, S. U.; Moussaid, A.; Pusey, P. N.; Schofield, A. B.; Cates, M. E.; Fuchs, M.; Poon, W. C. K. *Science* **2002**, *296* (5565), 104–106.
- (6) Manley, S.; Cipelletti, L.; Trappe, V.; Bailey, A. E.; Christianson, R. J.; Gasser, U.; Prasad, V.; Segre, P. N.; Doherty, M. P.; Sankaran, S.; Jankovsky, A. L.; Shiley, B.; Bowen, J.; Eggers, J.; Kurta, C.; Lorik, T.; Weitz, D. A. *Phys. Rev. Lett.* **2004**, *93* (10).
- (7) Lin, M. Y.; Lindsay, H. M.; Weitz, D. A.; Ball, R. C.; Klein, R.; Meakin, P. *Nature* **1989**, *339* (6223), 360–362.
- (8) Solomon, M. J.; Varadan, P. *Phys. Rev. E* **2001**, *6305* (5).
- (9) Vavrin, R.; Kohlbrecher, J.; Wilk, A.; Ratajczyk, M.; Lettinga, M. P.; Buitenhuis, J.; Meier, G. *J. Chem. Phys.* **2009**, *130* (15).
- (10) Sztucki, M.; Narayanan, T.; Belina, G.; Moussaid, A.; Pignon, F.; Hoekstra, H. *Phys. Rev. E* **2006**, *74* (5).
- (11) Verduin, H.; Dhont, J. K. G. *J. Colloid Interface Sci.* **1995**, *172* (2), 425–437.
- (12) Grant, M. C.; Russel, W. B. *Phys. Rev. E* **1993**, *47* (4), 2606–2614.
- (13) Zaccarelli, E. *J. Phys.: Condens. Matter* **2007**, *19* (32), 323101.
- (14) Meakin, P.; Stanley, H. E. *Phys. Rev. Lett.* **1983**, *51* (16), 1457–1460.
- (15) Meakin, P. *J. Colloid Interface Sci.* **1984**, *102* (2), 491–504.
- (16) Weitz, D. A.; Oliveria, M. *Phys. Rev. Lett.* **1984**, *52* (16), 1433–1436.
- (17) Chiew, Y. C.; Glandt, E. D. *J. Phys. A-Math Gen.* **1983**, *16* (11), 2599–2608.
- (18) Poon, W. C. K.; Haw, M. D. *Adv. Colloid Interface Sci.* **1997**, *73*, 71–126.
- (19) von Smoluchowski, M. *Z. Phys. Chem.* **1917**, *92* (2), 129–168.
- (20) Verwey, E. J. W.; Deboer, F.; Vansanten, J. H. *J. Chem. Phys.* **1948**, *16* (12), 1091–1092.
- (21) Russel, W. B.; Saville, D. A.; Schowalter, W. R. *Colloidal Dispersions*; Cambridge University Press: Cambridge, U.K., 1989.
- (22) Elliott, S. L.; Butera, R. J.; Hanus, L. H.; Wagner, N. J. *Faraday Discuss.* **2003**, *123*, 369–383.
- (23) Asakura, S.; Oosawa, F. *J. Polym. Sci.* **1958**, *33* (126), 183–192.
- (24) Lekkerkerker, H. N. W.; Poon, W. C. K.; Pusey, P. N.; Stroobants, A.; Warren, P. B. *Europhys. Lett.* **1992**, *20* (6), 559–564.
- (25) Shah, S. A.; Chen, Y. L.; Schweizer, K. S.; Zukoski, C. F. *J. Chem. Phys.* **2003**, *118* (7), 3350–3361.
- (26) Campbell, A. I.; Anderson, V. J.; van Duijneveldt, J. S.; Bartlett, P. *Phys. Rev. Lett.* **2005**, *94* (20).
- (27) Dinsmore, A. D.; Weitz, D. A. *J. Phys.: Condens. Matter* **2002**, *14* (33), 7581–7597.
- (28) Lu, P. J.; Conrad, J. C.; Wyss, H. M.; Schofield, A. B.; Weitz, D. A. *Phys. Rev. Lett.* **2006**, *96* (2).
- (29) Lu, P. J.; Zaccarelli, E.; Ciulla, F.; Schofield, A. B.; Sciortino, F.; Weitz, D. A. *Nature* **2008**, *453* (7194), 499–U4.
- (30) Poon, W. C. K. *J. Phys.: Condens. Matter* **2002**, *14* (33), R859–R880.
- (31) Iller, R. K. *Silica Hydrosol Powder*; Wiley and Sons: New York, 1957.
- (32) van Helden, A. K.; Jansen, J. W.; Vrij, A. *J. Colloid Interface Sci.* **1981**, *81* (2), 354–368.
- (33) Chen, M.; Russel, W. B. *J. Colloid Interface Sci.* **1991**, *141* (2), 564–577.
- (34) Woutersen, A.; May, R. P.; Dekruif, C. G. *J. Colloid Interface Sci.* **1992**, *151* (2), 410–420.
- (35) Jansen, J. W.; Dekruif, C. G.; Vrij, A. *J. Colloid Interface Sci.* **1986**, *114* (2), 481–491.
- (36) Eberle, A. P. R.; Wagner, N. J.; Akgun, B.; Satija, S. K. *Langmuir* **2010**, *26* (5), 3003–3007.
- (37) Roke, S.; Buitenhuis, J.; van Miltenburg, J. C.; Bonn, M.; van Blaaderen, A. *J. Phys.: Condens. Matter* **2005**, *17* (45), 3469–3479.
- (38) Penders, M.; Vrij, A.; Vanderhaegen, R. *J. Colloid Interface Sci.* **1991**, *144* (1), 86–97.
- (39) Penders, M.; Vrij, A. *Adv. Colloid Interface Sci.* **1991**, *36*, 185–217.
- (40) Narayanan, T.; Sztucki, M.; Belina, G.; Pignon, F. *Phys. Rev. Lett.* **2006**, *96*, 25.
- (41) Rueb, C. J.; Zukoski, C. F. *J. Rheol.* **1998**, *42* (6), 1451–1476.
- (42) Miller, M. A.; Frenkel, D. *Phys. Rev. Lett.* **2003**, *90* (13), 135702.
- (43) Vicsek, T. *Fractal Growth Phenomena*; World Scientific: Singapore, 1989.
- (44) Bergenholtz, J.; Poon, W. C. K.; Fuchs, M. *Langmuir* **2003**, *19* (10), 4493–4503.
- (45) Trappe, V.; Prasad, V.; Cipelletti, L.; Segre, P. N.; Weitz, D. A. *Nature* **2001**, *411* (6839), 772–775.
- (46) Kroy, K.; Cates, M. E.; Poon, W. C. K. *Phys. Rev. Lett.* **2004**, *92* (14).
- (47) Winter, H. H.; Chambon, F. *J. Rheol.* **1986**, *30* (2), 367–382.
- (48) Lide, D. R. *CRC Handbook of Chemistry and Physics*, 85th ed.; CRC Press: New York, 2004.
- (49) Berne, B. J.; Pecora, P. *Dynamic Light Scattering: With Applications to Chemistry, Biology, and Physics*; General Publishing Company, Ltd.: Toronto, 1976.
- (50) Takeda, M.; Norisuye, T.; Shibayama, M. *Macromolecules* **2000**, *33* (8), 2909–2915.
- (51) Cao, X. J.; Cummins, H. Z.; Morris, J. F. *Soft Matter* **2010**, *6* (21), 5425–5433.
- (52) Shibayama, M.; Norisuye, T. *B. Chem. Soc. Jpn.* **2002**, *75* (4), 641–659.
- (53) Norisuye, T.; Inoue, M.; Shibayama, M.; Tamaki, R.; Chujo, Y. *Macromolecules* **2000**, *33* (3), 900–905.
- (54) Martin, J. E.; Wilcoxon, J. P. *Phys. Rev. Lett.* **1988**, *61* (3), 373–376.
- (55) Martin, J. E.; Wilcoxon, J.; Odinek, J. *Phys. Rev. A* **1991**, *43* (2), 858–872.
- (56) Kline, S. R. *J. Appl. Crystallogr.* **2006**, *39*, 895–900.
- (57) Ornstein, L. S.; Zernike, F. *Proc. K. Ned. Akad. Wet. Amsterdam* **1914**, *17*, 793–806.
- (58) Percus, J. K.; Yevick, G. J. *Phys. Rev.* **1958**, *110* (1), 1–13.
- (59) Baxter, R. J. *J. Chem. Phys.* **1968**, *49* (6), 2770–8.
- (60) Muller, A.; Lonsdale, K. *Acta Crystallogr.* **1948**, *1* (1–6), 129–131.
- (61) Russel, W. B. *J. Chem. Soc., Faraday Trans. 2* **1984**, *80*, 31–41.
- (62) Roke, S.; Berg, O.; Buitenhuis, J.; van Blaaderen, A.; Bonn, M. *Proc. Natl. Acad. Sci.* **2006**, *103* (36), 13310–13314.
- (63) Guo, H.; Ramakrishnan, S.; Harden, J. L.; Leheny, R. L. *Phys. Rev. E* **2010**, *81*, (5).
- (64) Del Gado, E.; Fierro, A.; de Arcangelis, L.; Coniglio, A. *Phys. Rev. E* **2004**, *69*, (5).
- (65) Krall, A. H.; Weitz, D. A. *Phys. Rev. Lett.* **1998**, *80* (4), 778–781.
- (66) Mallamace, F.; Gambadauro, P.; Micali, N.; Tartaglia, P.; Liao, C.; Chen, S. H. *Phys. Rev. Lett.* **2000**, *84* (23), 5431–5434.
- (67) Hess, W.; Vilgis, T. A.; Winter, H. H. *Macromolecules* **1988**, *21* (8), 2536–2542.
- (68) Noro, M. G.; Frenkel, D. *J. Chem. Phys.* **2000**, *113* (8), 2941–2944.
- (69) Schaefer, D. W.; Martin, J. E.; Wiltzius, P.; Cannell, D. S. *Phys. Rev. Lett.* **1984**, *52* (26), 2371–2374.
- (70) Kegel, W. K.; van Blaaderen, A. *Science* **2000**, *287* (5451), 290–293.
- (71) Napper, D. H. *J. Colloid Interface Sci.* **1977**, *58* (2), 390–407.
- (72) Maranzano, B. J.; Wagner, N. J. *Rheol. Acta* **2000**, *39* (5), 483–494.
- (73) Kranendonk, W. G. T.; Frenkel, D. *Mol. Phys.* **1988**, *64* (3), 403–424.
- (74) Marr, D. W.; Gast, A. P. *J. Chem. Phys.* **1993**, *99* (3), 2024–2031.

- (75) Bergenholtz, J.; Fuchs, M. *Phys. Rev. E* **1999**, 59 (5), 5706–5715.
- (76) Frenkel, D. *Science* **2006**, 314 (5800), 768–769.
- (77) Poon, W. C. K.; Pirie, A. D.; Pusey, P. N. *Faraday Discuss.* **1995**, 101, 65–76.
- (78) Fuchs, M.; Schweizer, K. S. *J. Phys.: Condens. Matter* **2002**, 14 (12), R239–R269.